ADVANCED MATERIALS
www.advmat.de

Buried Interface Regulation with a Supramolecular Assembled Template Enables High-Performance Perovskite Solar Cells for Minimizing the V_{OC} Deficit

Zhenrong Wang, Qiong Liang, Mingliang Li, Guohao Sun, Shiang Li, Tao Zhu, Yu Han, Hao Xia, Zhiwei Ren, Bingcheng Yu, Jiyao Zhang, Ruijie Ma, Hrisheekesh Thachoth Chandran, Lei Cheng, Liren Zhang, Dongyang Li, Shuyan Chen, Xinhui Lu, Chang Yan, Randi Azmi, Kuan Liu,* Jinyao Tang,* and Gang Li**

Despite the rapid development of perovskite solar cells (PSCs) in the past decade, the open-circuit voltage (V_{OC}) of PSCs still lags behind the theoretical Shockley–Queisser limit. Energy-level mismatch and unwanted nonradiative recombination at key interfaces are the main factors detrimental to V_{OC}. Herein, a perovskite crystallization-driven template is constructed at the SnO_2/perovskite buried interface through a self-assembled amphiphilic phosphonate derivative. The highly oriented supramolecular template grows from an evolutionary selection growth via solid–solid phase transition. This strategy induces perovskite crystallization into a highly preferred (100) orientation toward out-of-plane direction and facilitated carrier extraction and transfer due to the elimination of energy barrier. This self-assembly process positively passivates the intrinsic surface defects at the SnO_2/perovskite interface through the functionalized moieties, a marked contrast to the passive effect achieved via incidental contacts in conventional passivation methods. As a result, PSCs with buried interface modification exhibit a promising PCE of 25.34%, with a maximum V_{OC} of 1.23 V, corresponding to a mere 0.306 V deficit (for perovskite bandgap of 1.536 eV), reaching 97.2% of the theoretical V_{OC} limit. This strategy spontaneously improves the long-term operational stability of PSCs under thermal and moisture stress (ISOS-L-3: MPP, 65 °C, 50% RH, T_{92} lifetime exceeding 1200 h).

1. Introduction

Lead halide perovskite solar cells (PSCs) have attracted intense attention and are considered to be the next-generation photovoltaic (PV) technologies due to their superior photoelectric properties, such as adjustable band gaps, high absorption coefficients, and long charge carrier diffusion lengths.[1–4] Over the past decade, the certified efficiency of single junction PSCs has increased rapidly from 3.8% to 26.7% with worldwide tremendous effort, which is comparable to those of market leader PV technologies.[5]

Despite their rapid development, as the core parameter, the open-circuit voltage (V_{OC}) of PSCs still lags behind the theoretical Shockley–Queisser (S–Q) limit.[6] Two main factors affect the V_{OC} of devices: energy-level mismatch and nonradiative recombination at key interfaces. Deep-level traps at the perovskite buried interface (e.g., under-coordinated lead cations, Pb–I antisite defects) serve as the nonradiative

Z. Wang, Q. Liang, G. Sun, T. Zhu, Y. Han, H. Xia, Z. Ren, B. Yu, J. Zhang, R. Ma, H. Thachoth Chandran, L. Cheng, D. Li, K. Liu, G. Li
Department of Electrical and Electronic Engineering
The Hong Kong Polytechnic University
Hung Hom, Kowloon, Hong Kong 999077, China
E-mail: kuan-lk.liu@polyu.edu.hk; gang.w.li@polyu.edu.hk

The ORCID identification number(s) for the author(s) of this article can be found under https://doi.org/10.1002/adma.202418011

DOI: 10.1002/adma.202418011

Z. Wang, R. Azmi
School of Science and Engineering
The Chinese University of Hong Kong
Shenzhen (CUHK-SZ), Guangdong 518172, China

M. Li, L. Zhang, J. Tang
Department of Chemistry
State Key Laboratory of Synthetic Chemistry
HKU-CAS Joint Laboratory on New Materials and Department of Chemistry
The University of Hong Kong
Hong Kong 999077, China
E-mail: liml@hku.hk; jinyao@hku.hk

S. Li, X. Lu
Department of Physics
The Chinese University of Hong Kong
New Territories, Sha Tin, Hong Kong 999077, China

recombination center, also detrimental to the device performance (especially V_{OC}) and accelerate the perovskite degradation under thermal and moisture stress.[7,8] On the other hand, for conventionally structured PSCs, the uncoordinated Sn^{2+} (Sn–OH) acts as shallow trap sites on the surface of the SnO_2 electron transport layer (ETL), which impairs the electron transfer efficiency between perovskite and ETL.[9,10]

It is widely recognized that the buried interface modification (e.g., via a molecular bridge, or self-assembled monolayers, SAMs), as a synergetic strategy, not only restrains the deep-level defects but enhances interface contact and aligns the mismatched energy levels.[11–13] Although multiple dipole molecules with two-sided coordinate effects have been selected to construct the robust contact and have shown promising results,[14,15] there is still much room to further improve the V_{OC} of PSCs.[16–19] In addition, the molecular arrangement and orientation of these interlayers at the buried interface have rarely been concerned, and their role as a template regulating the perovskite film formation and crystallization was often overlooked.[20,21]

In this work, we constructed a perovskite crystallization-driven template at SnO_2/perovskite buried interface through a self-assembled amphiphilic phosphonate derivative (MeOBTBT-POEt, as shown in **Figure 1a**. The weak interactions, e.g., π–π interactions and dipole–dipole interactions, present in supramolecular design, contribute to a substantial reduction in its phase-transition temperature, potentially reaching the window of room temperature, which in turn, facilitates the spontaneous assembly of long-range-order 2D single-crystalline morphology into a multilayered template, with a high degree of regularity even at room temperature.[22] The highly oriented MeOBTBT-POEt template is self-assembled from an evolutionary selection process via a solid–solid phase transition process and meanwhile induces the perovskite crystallization into a highly preferred orientation toward the out-of-plane direction. In addition, with a dipole moment of 1.89 D, this molecular bridge coordinates the interfacial energy level alignment and facilitates the electron extraction and transfer. The functionalized moieties in MeOBTBT-POEt spontaneously and positively restrain the oxygen vacancy of SnO_2 and under-coordinated defects in perovskite, thus suppressing the unwanted nonradiative recombination, a marked contrast to the passive effect achieved via incidental contacts, as observed in conventional passivation methods. As a result, the PSCs with buried interface modification (BIM) exhibit a promising PCE of 25.34% for n–i–p devices, with the maximum V_{OC} of 1.23 V, corresponding to a mere 0.306 V deficit (for perovskite bandgap of 1.536 eV), reaching 97.2% of the theoretical V_{OC} limit, which is among the highest in all perovskite systems. This strategy spontaneously improves the long-term operational stability of PSCs under thermal and moisture stress, delivering T_{92} lifetime exceeding 1200 h (ISOS-L-3: MPP, 65 °C, 50% RH).

2. Results And Discussion

The molecule, MeOBTBT-POEt, was obtained according to the synthetic route shown in Note S1, and Figure S1 (Supporting Information). Detailed synthetic procedures and data are available in Note S2, Figures S2–S8 (Supporting Information). MeOBTBT-POEt consists of a rigid π-backbone benzothieno[3,2-b][1]benzothiophene (BTBT) and a flexible phosphonate-engineered alkyl tail with the superior self-assembly property. We obtained the single crystal of the head group of MeOBTBT-POEt through a solvent evaporation method and analyzed its crystallographic data (Figure S9,Supporting Information). It belongs to monoclinic lattice (a = 25.866 Å, b = 5.8244 Å, c = 8.0498 Å, $\alpha = \gamma = 90°$, $\beta = 90.835°$). Figure S10 (Supporting Information) shows the UV-vis absorption spectrum of MeOBTBT-POEt solution, which is a relatively large bandgap organic semiconductor with an absorption band edge of ≈370 nm (3.35 eV), and thus has negligible impact on the parasitic absorption at the buried interface. Supramolecular assembly is the dynamic process in which molecules of a system organize themselves into ordered patterns or structures through noncovalent interactions.[23] Between phosphate groups of MeOBTBT-POEt, there exists a weak dipole–dipole interaction, which helps to synergistically operate with the intermolecular π–π interaction and van der Waals forces. These weak interactions lower the phase-transition temperature, even approaching the room temperature window, and thus facilitate the spontaneous self-assembly of long-range-order 2D morphology in high regularity at room temperature. This stands in stark contrast to SAMs, which are extensively utilized and whose deposition is primarily dependent on chemisorption with the substrate. This implies that the substrate substantially impacts the properties of these monolayer microstructures, necessitating further post-processing for the optimal packing of head groups. The obtained ordered microstructures can work as ideal templates for the fabrication of regular superstructures above.[24,25] Herein, we take advantage of the room-temperature supramolecular assembly properties of the amphiphilic phosphonate derivatives, MeOBTBT-POEt, to serve as a template favored for perovskite crystallization and molecular bridge at the buried interface of PSCs.

The thermal stability of MeOBTBT-POEt was evidenced by thermogravimetric analysis (TGA, Figure S11a, Supporting Information). The room-temperature supramolecular-assembly properties were first validated by differential scanning calorimetry (DSC) tests, as the peak at 94 °C (from stable to meta-stable phase) remained in the first heating round for both the fresh

S. Chen, C. Yan
Sustainable Energy and Environment Thrust
The Hong Kong University of Science and Technology (Guangzhou)
Guangzhou, Guangdong 511400, China
K. Liu, G. Li
Research Institute for Smart Energy (RISE)
The Hong Kong Polytechnic University
Hung Hom, Kowloon, Hong Kong 999077, China
J. Tang
Materials Innovation Institute for Life Sciences and Energy (MILES)
HKU-SIRI
Shenzhen 518000, China
G. Li
Photonics Research Institute (PRI)
The Hong Kong Polytechnic University
Hung Hom, Kowloon, Hong Kong 999077, China
G. Li
Guangdong-Hong Kong-Macao Joint Laboratory for
Photonic-Thermal-Electrical Energy Materials and Devices
The Hong Kong Polytechnic University
Hung Hom, Kowloon, Hong Kong 999077, China

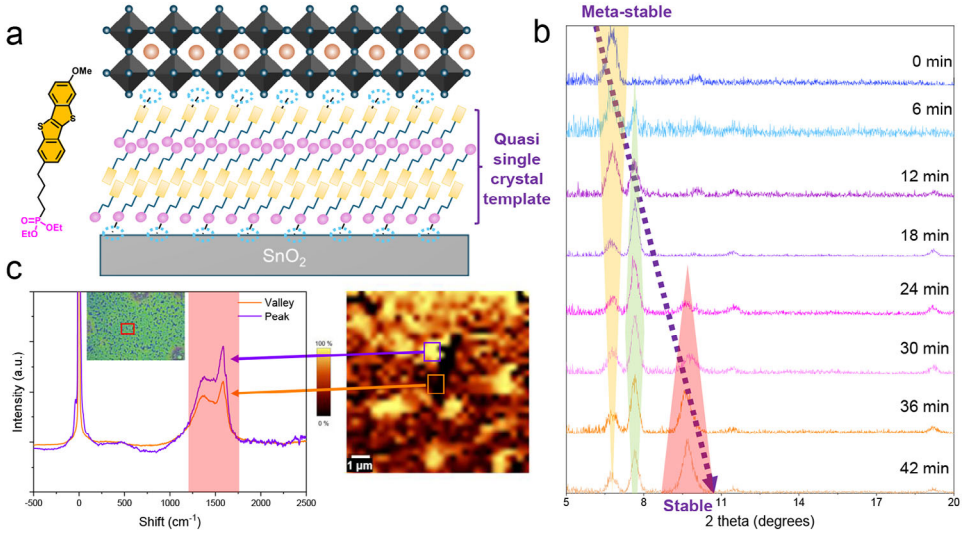

Figure 1. a). Schematic diagram of multilayered MeOBTBT-POEt supramolecular assembled template between SnO_2 and perovskite films. b) In situ X-ray diffraction (XRD) spectroscopy during the accelerated solid–solid transition of MeOBTBT-POEt. c) Raman spectroscopy and corresponding 2D intergral mapping (from 1200 to 1750 cm^{-1}) for MeOBTBT-POEt modified SnO_2.

samples and the melt samples in the same crucible kept for 7 days at room temperature (Figure S11b,c, Supporting Information). To further verify the supramolecular assembly on SnO_2 substrate via solid–solid transition, we performed in situ X-ray diffraction (XRD) spectroscopy on as-cast films of MeOBTBT-POEt to monitor the crystal structure evolution during thermal annealing at 60 °C, a process where heating can speed up the solid–solid transition. Each XRD pattern was recorded in the 2θ region of 5–50°at 9°/min of scan rate. As observed in Figure 1b, the peaks exhibited distinct variations of intensity during the accelerated transition process. This meta-stable peak (indicated yellow area) progressively diminished with time, while a pair of new Bragg peaks (highlighted by green and red areas) emerged at increased angles beside the original peak. It's worth noting that the peak intensity at 7.7° increased at the beginning and then diminished gradually, which indicates it is also an intermediate phase and could finally evolve into a stable phase, as evidenced by the peak at 9.8°. Moreover, the peak shift to the higher 2θ could also evidence a closer supramolecular packing evolution into a new regular polymorph, which could benefit the templating for perovskite film formation.

To prove the surface coverage of MeOBTBT-POEt film on SnO_2 ETL, Raman spectroscopy was performed with similar morphologies for both the pristine and modified SnO_2 (Figure 1c; Figure S12, Supporting Information). The characteristic peak of BTBT core at 1590 cm^{-1} can be observed from the modified samples in both the valley and peak in 2D integral mapping, which indicates full coverage and uniformity of the molecular bridge on the substrate from its amorphous state.[26] To delve deeper into their crystalline characteristics, a 2D grazing-incidence wide-angle X-ray scattering (2D-GIWAXS) was carried out (as seen in **Figure** 2a) after the supramolecular assembly on SnO_2 ETL. This analysis revealed a number of high-order spots in the q_z direction (out-of-plane) for a specified q_{xy} (in-plane). The detection of Bragg reflections up to the 14th order suggests a quasi-single-crystalline structure, which stands in stark contrast to the observed polycrystalline films that generate scattered diffusion around the Debye ring.[27]

The perovskite film was subsequently deposited onto the as-cast MeOBTBT-POEt modified substrate. It should be noted that MeOBTBT-POEt has very limited solubility in the mixed dimethyl formamide/dimethyl sulfoxide (DMF/DMSO = 4:1, v:v), even at a very low concentration (1 mg mL^{-1}), whereas it shows good solubility into chlorobenzene (CB, 20 mg mL^{-1}, Figure S13, Supporting Information), which means that the sequential deposition of perovskite would not damage the as-cast MeOBTBT-POEt film (Figure S14, Supporting Information). The time-of-flight secondary ion mass spectrometry (ToF-SIMS) result also confirms that MeOBTBT-POEt is mainly distributed at the buried interface between perovskite and SnO_2 ETL (Figure S15, Supporting Information). We analyzed the crystal orientation for the final perovskite films through GIWAXS. Figure 2b shows the 2D GIWAXS patterns for the perovskite grown upon the pristine and MeOBTBT-POEt-modified SnO_2 measured under incident angles (a_i) of 1°. Figure 2c shows the polar intensity profiles along the (100) ring at q_z = 1.00 A^{-1} from the 2D GIWAXS patterns of these two types of perovskite films. The perovskite grown on the pristine SnO_2 exhibits almost an isotropic (100) ring, with a slightly preferred orientation at ± 63.5°, while the (100) ring of the perovskite grown on MeOBTBT-POEt-modified SnO_2 concentrates along the out-of-plane (q_z) direction (close to 0°). This result indicates that the supramolecular assembly from meta-stable to stable phase simultaneously induced the perovskite crystallization into a highly preferred orientation toward out-of-plane direction. It suggests a relatively dominant out-of-plane orientation with respect to the substrate for the perovskite grains, which is supposed to facilitate charge transport of PSCs in the vertical direction.[28,29]

In order to investigate the mechanism of MeOBTBT-POEt on perovskite facet orientation, we performed the density functional theory (DFT) calculations to estimate its interaction with Pb–I frameworks of $FAPbI_3$ along different crystal facets

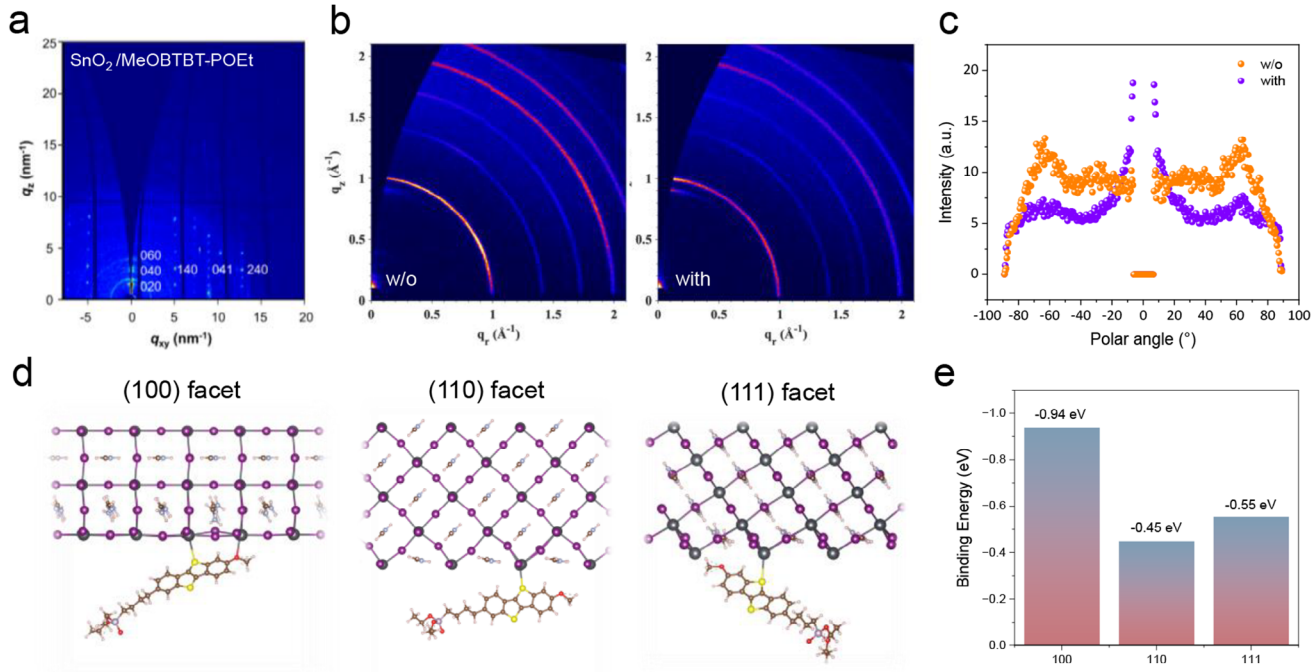

Figure 2. a). 2D grazing-incidence wide-angle X-ray scattering (2D GIWAXS) of MeOBTBT-POEt on SnO_2 substrate. b) 2D GIWAXS patterns for the perovskite films grown upon the pristine and MeOBTBT-POEt-modified SnO_2. c) Polar intensity profiles along the (100) ring at q_z = 1.00 A^{-1} for the perovskite films grown upon the pristine and MeOBTBT-POEt-modified SnO_2. d) Optimized binding models of MeOBTBT-POEt on (100), (110), and (111) perovskite facets along the *x*-axis, respectively. e) Calculation of the corresponding binding energies.

(more details in Note S3, and Figure S16, Supporting Information). Figure 2d shows the optimized binding models of MeOBTBT-POEt on (100), (110), and (111) perovskite facets along the *x*-axis, respectively. We calculate their corresponding binding energy (E_b), as shown in Figure 2e. Compared with much smaller E_b of −0.45 and −0.55 eV on (110) and (111) facets, respectively, MeOBTBT-POEt shows the strongest interaction with (100) facet, with the largest E_b of −0.94 eV. This result indicates that during the perovskite crystallization process, MeOBTBT-POEt will selectively attach to (100) facet of $FAPbI_3$ nuclei via the strong chemical interactions, thereby reducing its surface energy, and further providing an additional thermodynamic driving force to promote its preferential crystal growth and lead to a (100)-dominated orientation in the out-of-plane direction.

The crystal structure of the final perovskite films was also analyzed, as shown in Figure S17 (Supporting Information). Both of them display similar diffraction patterns, with a set of sharp peaks typical for the cubic $FAPbI_3$ phase (Pm3m). A small PbI_2 diffraction peak at 2θ = 12.67° is also observed in both samples because of 5 mol% excess PbI_2 in the perovskite precursor recipe. It has been suggested that a moderate residue of excess PbI_2 can passivate the defects at perovskite surface and grain boundaries (GBs), thus enhancing the device's performance.[30,31] After buried interface modification with MeOBTBT-POEt, the XRD patterns show an increased ratio of the intensities between (100) at 2θ = 14.06° and (111) at 2θ = 24.48° from 5.87 to 8.65, coincident with the result from GIWAXS. Subsequent investigation focused on elucidating the impact of MeOBTBT-POEt modification on the morphology of perovskite films. Scanning electron microscopy (SEM) provided visual insights, with comparative images of perovskite films grown on the pristine and modified SnO_2, as shown in Figure S18 (Supporting Information). We observed a larger domain size for the perovskite on modified SnO_2, which may attribute to the retarded crystallization process since it requires more energy for heterogeneous nucleation on a BTBT-terminated hydrophobic surface.[28,32,33]

To investigate how MeOBTBT-POEt treatment influences the chemical environment of the underlying SnO_2 ETL, we first examined their interaction via X-ray photoelectron spectroscopy (XPS). As shown in Figure S19a (Supporting Information), the P 2p signal at 137.3 eV confirms the presence of MeOBTBT-POEt (diethylphosphonate moieties) on the SnO_2 surface. The Sn $3d_{3/2}$ peak at 495.55 eV and Sn $3d_{5/2}$ at 487.17 eV for pristine SnO_2 film shift to 495.30 eV and 486.92 eV, respectively, after MeOBTBT-POEt modification, which indicates an increased electron density at the Sn atom, which is attributed to the coordinate interaction with MeOBTBT-POEt (**Figure 3a**). We observed decoupled O 1s signals of pristine SnO_2 films into two peaks at 530.99 eV and 532.36 eV (Figure 3b). The peak at lower binding energy originated from Sn–O–Sn backbones serving as electron conductance pathways, and the peak at higher binding energy belongs to the hydroxide species (Sn–OH), which is well recognized to act as shallow trap sites.[9,34,35] More importantly, MeOBTBT-POEt effectively suppresses the hydroxide species (Sn–OH), according to the integrated areas ratio for Sn^{4+}/Sn^{2+} from 3.45 to 35.25, after modification. These XPS results imply the chemical interactions between MeOBTBT-POEt and SnO_2, which originate from the triethyl phosphonate group coordinating with the undercoordinated Sn^{2+}.

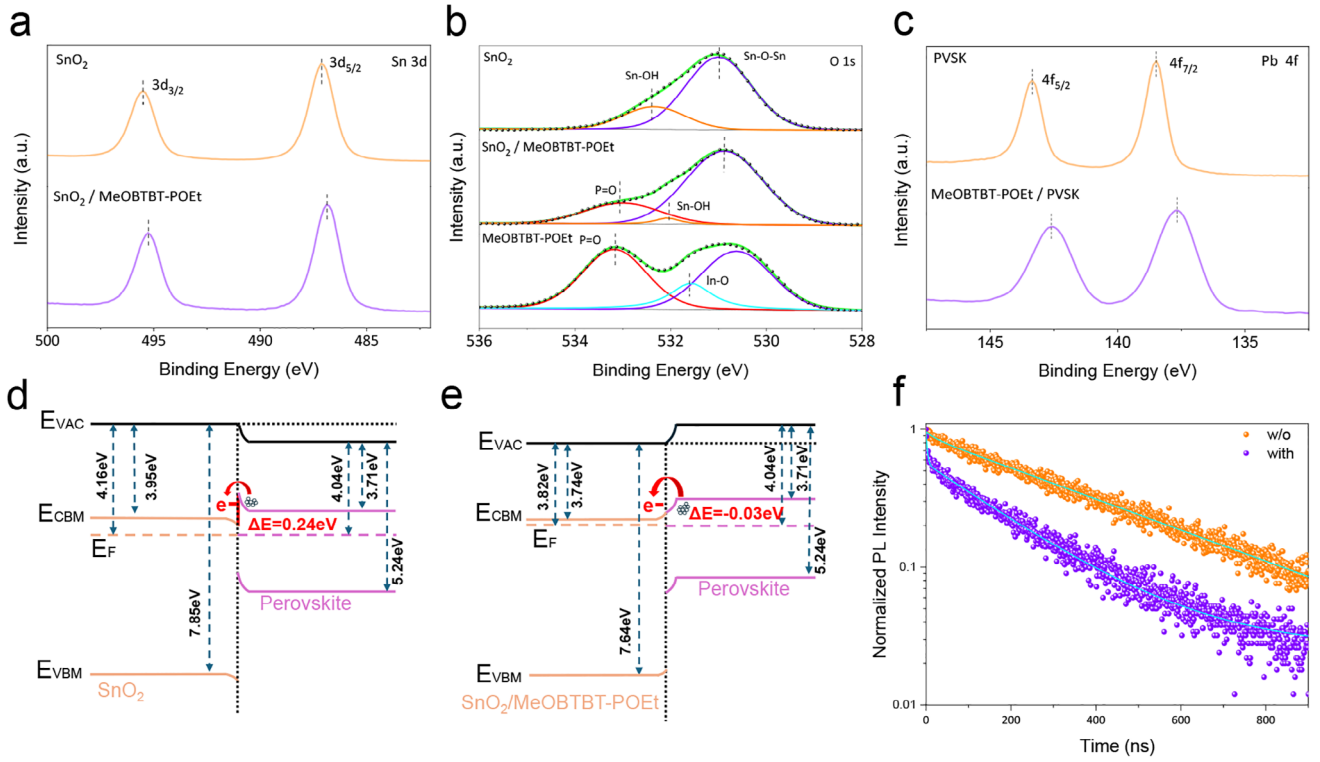

Figure 3. a). Sn 3d X-ray photoelectron spectroscopy (XPS) spectra of SnO_2, MeOBTBT-POEt modified SnO_2, respectively. b) Pb 4f XPS spectra of perovskite and the buried MeOBTBT-POEt/Perovskite, respectively. c) O 1s XPS spectra of SnO_2, MeOBTBT-POEt modified SnO_2, and MeOBTBT-POEt, respectively. Band structure of d) SnO_2/Perovskite, and e) MeOBTBT-POEt modified SnO_2/Perovskite interface. f) Time-resolved photoluminescence (TRPL) decays of perovskite films grown upon the pristine and MeOBTBT-POEt-modified SnO_2.

We also examined the XPS of a buried interface between MeOBTBT-POEt and perovskite films through the physical detaching method. Pb 4f spectra of the pristine perovskite film exhibit two prominent peaks at 138.49 and 143.34 eV, corresponding to Pb $4f_{7/2}$ and Pb $4f_{5/2}$, respectively. (Figure 3c) Compared with the pristine, the Pb 4f peaks for the MeOBTBT-POEt/perovskite sample show a downward shift in binding energy (137.65 and 142.62 eV), indicating the strong coordinate interaction between MeOBTBT-POEt and perovskites. In addition, we observed a S 2p signal of MeOBTBT-POEt/perovskite film with the identical shape as that for the pristine MeOBTBT-POEt, accompanied by a shift toward the lower binding energy (Figure S19b, Supporting Information). This result indicates that the deposition of perovskite films upon MeOBTBT-POEt would not affect the underlying modified interlayer and verifies the coordinate interaction between MeOBTBT-POEt and the perovskite layer. XPS results verify the spontaneous passivation effects on oxygen vacancy in SnO_2 and under-coordinated Pb^{2+} in perovskite.

The electrostatic potential (ESP) of the molecule was calculated by DFT, as shown in Figure S20 (Supporting Information). The gradual shift in color from red to blue depicted in the ESP map signifies a corresponding increase in electron density from the phosphonate group to the BTBT core. This observation suggests that the MeOBTBT-POEt molecule has a high dipole moment of 1.89 D and is a viable candidate for the surface modification of SnO_2.[36] (Figure S21, Supporting Information). We performed ultraviolet photoemission spectroscopy (UPS) to evaluate the band structure at the electron selective interface, and examined the energy level of pristine SnO_2, MeOBTBT-POEt-modified SnO_2, and perovskite films, as shown in Figure S22 (Supporting Information). After MeOBTBT-POEt modification, the secondary electron cutoff ($E_{cut\text{-}off}$) edge of SnO_2 shifts from 17.06 to 17.40 eV, corresponding to an up-shift of work function (E_F) from 4.16 to 3.82 eV, which mainly ascribes to the negative dipole of MeOBTBT-POEt inward. We further calculated the valence band maximum (E_{VBM}) of SnO_2 and modified SnO_2 to be 8.00 and 7.64 eV, respectively. Combining with the bandgap from the Tauc plot of UV–vis absorption, their conduction band minimum (E_{CBM}) was calculated to be 4.16 and 3.74 eV, respectively, for pristine and modified SnO_2. All energy levels are summarized in Table S1 (Supporting Information), and the schematic energy level diagrams of this elective interface are depicted in Figure 3d,e.

This intrinsic dipole moment at SnO_2/perovskite affected their band structure and corresponding carrier transfer dynamics. After the MeOBTBT-POEt modification, the E_{CBM} of SnO_2 (3.74 eV) exhibits a minor upward shift, bringing it closer to the perovskite E_{CBM} (3.71 eV) in comparison to the control SnO_2 E_{VCB} (3.95 eV). This change is anticipated to yield benefits in terms of reducing the energy barrier at the interface, consequently suppressing interface recombination. Furthermore, the dipole effect of the MeOBTBT-POEt bridge is also substantiated by the observed change in SnO_2's work function, which shifts from 4.16 to

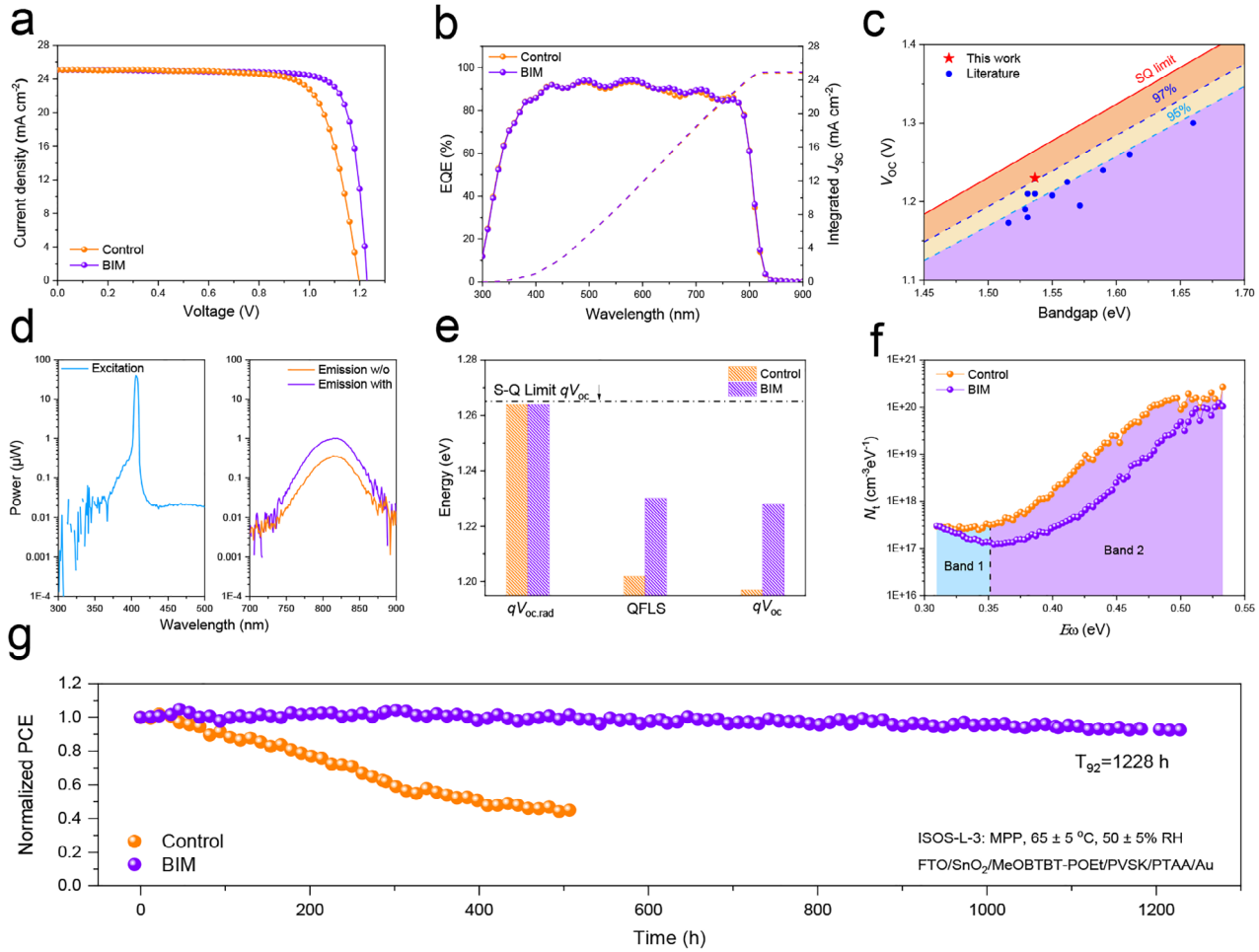

Figure 4. a). *J–V* curves of the best-performance control and BIM-based devices. b) External quantum efficiency (EQE) spectra of the control and BIM-based devices. c) Comparison of the V_{OC} in this work with the state-of-the-art values and their corresponding bandgaps from the literature.[41,51–61] d) Photoluminescence quantum yields (PLQYs) of the SnO_2/perovskite half stacks without or with MeOBTBT-POEt modification. e) Quasi-Fermi level splitting (QFLS) analysis for the control and BIM-based devices. f) Energetic distribution of trap density of states measured by thermal admittance spectroscopy. g) Long-term operational stability test (ISOS-L-3: MPP, 65 °C, 50% RH).

3.82 eV post-modification. The electron extraction/transfer barrier between perovskite and SnO_2 ($\Delta E = E_{CB}{}^{PVSK} - E_{CB}{}^{SnO_2}$) is reduced from 0.24 to −0.03 eV, which suggests that the oriented MeOBTBT-POEt bridge at the buried interface is beneficial for electron extraction and transfer.

Time-resolved photoluminescence (TRPL) was further carried out to investigate the interfacial charge transfer dynamics (Figure 3f). Fitting the experimental data with the bi-exponential function $(I(t) = A_1 \exp(-\frac{t}{\tau_1}) + A_2 \exp(-\frac{t}{\tau_2}))$ and the fitting parameters are summarized in Table S2 (Supporting Information). It should be noted that the excitation fluence in our study is very low (≈5 nJ cm^{-2}), which only generates a much lower density of free carriers (≈2×10^{14} cm^{-3}) compared with that of trap states (≈10^{18} cm^{-3}). In this condition, TRPL decay mainly responds to charge separation and extraction.[37,38] Compared with the perovskites on pristine SnO_2 (381.7 ns), those on MeOBTBT-POEt-modified SnO_2 show a shorter average carrier lifetime with MeOBTBT-POEt modification (183.9 ns), which points toward an efficient electron extraction and transfer from perovskite to the SnO_2 ETL with the treatment of MeOBTBT-POEt.

Table 1. Photovoltaic parameters of the representative control and BIM-based devices.

Condition	V_{OC} [V]	J_{SC} [mA cm^{-2}]	FF [%]	PCE [%]	
				Average	Best
Control	1.197	25.08	75.99	22.24 ± 0.29	22.81
BIM	1.228	25.10	82.28	24.87 ± 0.26	25.34

We fabricated the conventional n–i–p PSCs assembled with the structure of FTO/SnO_2 /MeOBTBT-POEt/perovskite/spiro-OMeTAD/Au via the buried interface treatment with MeOBTBT-POEt. **Figure** 4a shows the *J–V* curves of the best-performance BIM-based devices treated by MeOBTBT-POEt solution under different concentrations, and **Table** 1 summarizes their

photovoltaic characteristics. Along with the concentrations from 0 to 2 mg mL^{-1}, their V_{OC} exhibits an increasing trend from 1.197 to 1.230 V (Table S3, Supporting Information), which is mainly attributed to the optimized band alignment and efficient passivation of intrinsic defects at the buried interface. At the same time, J_{SC} is almost kept constant at ≈25.1 mA cm^{-2}, which agrees well with the integrated J_{SC} from external quantum efficiency (EQE) spectra (Figure 4b, within 1% mismatch). Further increase in concentrations (from 2 to 10 mg mL^{-1}) would be detrimental to V_{OC} and FF, which is mainly attributed to the inferior carrier transport (Figures S23,S24, and Table S3, Supporting Information). Among them, the BIM-based devices with 1 mg mL^{-1} MeOBTBT-POEt treatment deliver the best performance, with a maximum PCE of 25.34%, as shown in Figure 4a and Table 1, without obvious hysteresis effect in *J*–*V* measurement (Figure S25, Supporting Information).

More importantly, compared with the control devices, the BIM-based devices under the optimized conditions demonstrated a pronouncedly enhanced V_{OC} and FF, which mainly ascribes to the improved band alignment and suppressed nonradiative energy loss. The photovoltaic bandgap (E_g^{PV}) of the FA-dominated perovskite used in this work was calculated to be ≈1.536 eV from the first differential of EQE spectra (Figure S26, Supporting Information). As far as we know, 1.23 V V_{OC} is one of the highest reported values in this bandgap of perovskite, and the corresponding V_{OC} deficit (0.306 V) is among the lowest in all perovskite systems (Table S4, Supporting Information). It is noteworthy that the V_{OC} of our devices reached 97.2% of the theoretical V_{OC} limit, as demonstrated in Figure 4c.

To analyse the fundamental mechanism underlying charge recombination and V_{OC} deficit, we identify the origins of increased V_{OC} in the BIM-based devices by quantifying the dominating recombination mechanisms using the electroluminescence method. We examined the external quantum efficiency of electroluminescence (EQE_{EL}) for a complete PSC operating as a light-emitting diode (LED) in forward voltage bias.[39–41] (Figure S27, Supporting Information). The V_{OC} difference should be originated from the nonradiative recombination loss ($\Delta V_{OC,nr}$), which can be calculated from the EQE_{EL} at the injection current density equal to J_{SC} with the equation ($\Delta V_{OC,nr} = -(\frac{k_B T}{q}) \times \ln EQE_{EL}$). Compared with the control device (EQE_{EL} = 2.73%, $\Delta V_{OC,nr}$ = 93.1 mV), The optimized BIM-based device exhibits a much enhanced EQE_{EL} of 10.29% at ≈25.1 mA cm^{-2} injection, corresponding to a $\Delta V_{OC,nr}$ of 58.8 mV, which is coincident with the V_{OC} deficit from *J*–*V* test. Our result indicates that this strategy significantly suppresses the nonradiative recombination at the buried interface between SnO_2 and perovskite, which dominates the V_{OC} enhancement for BIM-based devices.

We also derived the quasi-Fermi-level splitting (QFLS) from the analysis of PL, in order to further validate the V_{OC} deficit. The theoretical radiative limit of V_{OC} ($V_{OC,rad}$) was calculated from a detailed balance model:

$$V_{OC,rad} = \frac{k_B T}{q} \ln\left(\frac{\int EQE_{PV}(E) \times \phi_{AM1.5}(E)\, dE}{\int EQE_{PV}(E) \times \phi_{BB}(E)\, dE} + 1\right) = \frac{k_B T}{q} \ln\left(\frac{J_{SC}}{J_0^{rad}} + 1\right) \quad (1)$$

in which $\phi_{AM1.5}$ and ϕ_{BB} refer to the solar AM 1.5G spectrum and the black-body radiation spectrum at 300 K, respectively.[42,43] We derived the dark radiative recombination current ($J_{0,rad}$) of 1.43 × 10^{-20} mA cm^{-2}, and the $V_{oc,rad}$ of 1.264 V (Figure S28, and Table S5, Supporting Information). Photoluminescence quantum yield (PLQY) is indicative of solar cell behavior at the open-circuit condition; maximized PL in these half-stacks is crucial for achieving higher photovoltages due to reducing nonradiative recombination losses. We examined a notable increase in PLQY for the SnO_2/perovskite half stacks modified with MeOBTBT-POEt (from 9.09% to 27.06%), as shown in Figure 4d. The quasi-Fermi level splitting (QFLS) is determined by the following equation:

$$QFLS = qV_{oc,rad} + k_B T \ln(PLQY) \quad (2)$$

Combining the value of $qV_{oc,rad}$ (Table S5, Supporting Information), and QFLS for the SnO_2/perovskite half stacks, we elucidated the origins of the low V_{OC} deficit in our BIM-based devices. There is a substantially decreased energy loss, according to $\Delta(V_{OC,rad} - QFLS)$, from 62 to 34 meV (Figure 4e; Table S5, Supporting Information). From QFLS analysis, we conclude that the origin of the ultralow V_{OC} deficit is primarily attributed to the efficient elimination of nonradiative recombination at the buried interface between SnO_2 and perovskite.

We further measured the light intensity–V_{OC} relationship in the range from 10 to 100 mW cm^{-2}, as shown in Figure S29a (Supporting Information). The ideality factor (*n*) is correlated with the slope of the V_{OC} versus light intensity in the natural logarithm scale. The BIM-based devices show a smaller ideality factor of 1.12 compared with that of the control devices (*n* = 1.38). On the other hand, the FF loss between the Shockley–Queisser limit (FF_{SQ}) and the measured FF from *J*–*V* curves comprises two parts—nonradiative loss and charge transport loss. Following the detailed balanced model, FF_{SQ} is calculated to be 90.15% in the 1.53 eV perovskite system, and the maximum FF (FF_{max}) without charge transport loss can be calculated through the equation:

$$FF_{max} = \frac{\nu_{oc} - \ln(\nu_{oc} + 0.72)}{\nu_{oc} + 1} \quad (3)$$

in which $\nu_{oc} = \frac{V_{oc} q}{n k_B T}$. As shown in Figure S29b (Supporting Information), the enhanced FF for BIM-based devices comes from both the suppression of charge transport loss and non-radiative loss.

In order to further unravel the underlying carrier recombination and transfer dynamics, we performed the transient photovoltage (TPV) and transient photocurrent (TPC) analysis (Figure S30a,b, Supporting Information). The photovoltage signal is triggered by a pulse light that pumps up the carrier density and quasi-Fermi level splitting, and charge recombination is directly measured via monitoring the photovoltage decay.[44] Fitted by bi-exponential decay function, the BIM-based device exhibits a prolonged average decay time (τ_{TPV} = 133.34 µs), compared with that of the control device (61.87 µs), which suggests that less trap-assisted recombination in the BIM-based device, especially at the buried interface. In the TPC results, the BIM-based device exhibits a higher nonequilibrium carrier concentration collected at

both electrodes in total, compared with that of the control device under the same intensity of the pulse laser, which is determined by the integrated area of TPC curves. The enhanced nonequilibrium carrier concentration is mainly attributed to efficient transfer and collection at the electron selective interface.[45] Moreover, the photocurrent decay time (τ_{TPC}) for the BIM-based device is reduced from 0.86 to 0.73 µs, which is also in good agreement with the TRPL results.

Due to the ionic nature of perovskite materials, mobile ions (ionic conduction) during the space–charge limited current (SCLC) measurement often affect its electrical characterization and make the result inaccurate. We performed the pulsed voltage (PV)-SCLC technique as shown in Figure S31a (Supporting Information), which helps to localize the ion motion and deliver reproducible and reliable *J–V* characteristics without hysteresis, to estimate the electron trap density (N_{trap}). We followed the testing protocol from the previous work,[46] and obtained hysteresis-free SCLC curves under forward and reverse scanning, as shown in Figure S31b,c (Supporting Information). The trap-filled limit voltage (V_{TFL}) determined as the onset voltage of TFL regime ($n > 3$) can be used to calculate N_{trap} ($N_{trap} = \frac{2\epsilon_r\epsilon_0 V_{TFL}}{qL^2}$)[47] in which q represents the elementary charge, ϵ_r, and ϵ_0 are the relative dielectric constant (18 for hybrid perovskite materials) and vacuum permittivity, respectively. N_{trap} was estimated to be 1.02×10^{16} cm^{-3} and 0.66×10^{16} cm^{-3} for the control and BIM-based devices, respectively, indicating a substantial reduction of trap states.

Mott–Schottky analysis and thermal admittance spectroscopy (TAS) were further performed to quantitatively estimate the energetic distribution of trap density of states (tDOS). The fitting data from capacitance–voltage measurement indicates that BIM-based devices exhibit a V_{bi} of 1.10 V, which is larger than that of the control device (1.06 V), as shown in Figure S32 (Supporting Information). This trend agrees with the result from the QFLS analysis. In the TAS result, compared with the control device, the BIM-based devices display one order of magnitude lower trap density of states (as shown in Figure 4f, $E_\omega > 0.36$ eV, deep level, more details in Note S4, Supporting Information). It is well known that deep defects at perovskite surfaces and GBs are mainly regarded as nonradiative recombination centers, which is significantly detrimental to the V_{OC} of PSCs. This strategy not only manipulates the perovskite orientation through the favored template, delivering high-quality perovskite crystal, but also relieves these intrinsic defects by two times (9.62×10^{17} cm^{-3} vs 3.30×10^{17} cm^{-3}) via the efficient buried interface modification. Our strategy synergistically eliminates the intrinsic deep defects to a great extent and pushes the V_{OC} value close to the radiative limit.

For long-term stability, we monitored the PCE evolution for the control and BIM-based devices under MPP tracking and continuous 1-sun illumination under thermal and moisture stress (ISOS-L-3: 65 ± 5 °C, 50 ± 5% RH, PTAA-based n–i–p devices with the initial PCE = 19.20% and 20.88%, respectively, as shown in Figure S33, Supporting Information). BIM-based devices maintained over 92% of their initial PCE after 1228 h of operation at 65 °C (Figure 4g). It's well known that shallow defects (with low migration activation energy) at perovskite surface and grain boundaries initialize the permeation of moisture and oxygen into the perovskite films to accelerate the degradation of PSCs.[9,48–50] The effective relief of shallow defects and superior moisture resistance through our strategy is responsible for enhanced stability under different aging conditions.

3. Conclusion

In summary, we developed a buried interface regulation strategy using a supramolecular assembled template for improving the performance of PSCs. The quasi single-crystalline MeOBTBT-POEt template assembles from an evolutionary selection growth via the solid–solid phase transition process and thus spontaneously induces the perovskite crystallization into highly preferred (100) orientation toward out-of-plane direction. In addition, the MeOBTBT-POEt dipole eliminates the interface energy barrier and thus improves electron extraction and transfer. This molecular bridge also shows a strong chemical interaction at the buried interface between perovskite and SnO_2 to actively passivate the intrinsic defects, which is easier and more effective than the passive passivation via incidental contacts in traditional insertion-layer methods. As a result, the BIM-based devices achieved a promising PCE of up to 25.34%, with a maximum V_{OC} of 1.23 V, corresponding to a mere 0.306 V deficit. This strategy significantly improved the long-term operational stability of PSCs under thermal and moisture stress. This work offers a novel perspective of interface modification methods to push the PSCs closer to the S–Q limit.

4. Experimental Section

Materials: The following chemicals and solvents were used without further purification: lead iodide (PbI_2) (Sigma–Aldrich, 99.99%), lead(II) bromide ($PbBr_2$) (Sigma–Aldrich, 99.999%), formamidinium iodide (FAI) (Greatcell Energy), methylammonium bromide (MABr) (Greatcell Energy), and methylammonium chloride (MACl). All of the solvents were bought from Sigma–Aldrich, including dimethyl sulfoxide (DMSO) and N,N-dimethylformamide (DMF) (99.8%, anhydrous). Acyl chloride, sodium methoxide, Copper(I) iodide, Aluminium(III) chloride, 4-bromobutanoyl chloride, Lithium aluminum hydride, and Triethyl phosphite were purchased from TCI.

Device fabrication: FTO/glass substrates with laser patterns (sheet resistance ≈ 12 Ω per square) were cleaned in detergent, distilled water, acetone, and isopropanol, respectively. After 20 min of ultraviolet–ozone treatment, a thin coating of self-produced SnO_2 solution was spin-coated onto the FTO substrates at 4000 rpm. Then, it was annealed for 60 mins at 200 °C in an ambient atmosphere. The substrates were transferred into the glovebox. MeOBTBT-POEt was dissolved into CB with different concentrations (from 0 to 10 mg mL^{-1}) and spin-coated onto SnO_2 ETL. The mixed powders of FAI:MABr:MACl:$PbBr_2$:PbI_2 (molar ratio = 1.41:0.04:0.4:0.04:1.47) in DMF/DMSO (4:1, *v:v*) were combined with appropriate amount of CsI mother solution (1.5 M, in DMSO) stock solution to create the $Cs_{0.03}(FA_{0.97}MA_{0.03})_{0.97}Pb(I_{0.97}Br_{0.03})_3$ perovskite precursor solution (bandgap = 1.53 eV). The as-cast perovskite films were transferred into a controlled ambient environment (from 20% to 30% relative humidity, RH) and annealed onto a hotplate at 100 °C for 60 mins to facilitate the spontaneous cross-linking and perovskite crystallization. The samples were transferred into the glovebox and spin-coated with BABr (2 mg mL^{-1}, IPA) and spiro-OMeTAD (80 mg mL^{-1} in Chlorobenzene (CB), 29 µL of tBP, and 17.5 µL of Li-TFSI mother solution), respectively, followed by a 10 min annealing at 100 °C. An 80 nm thick Au electrode was subsequently patterned by thermally evaporating on top of the device using a shadow mask.

Characterizations: The single crystals were obtained based on a solvent evaporation method using a mixed solvent recipe (toluene and chloroform). The single crystals were measured by the Bruker D8 Venture Single Crystal Diffractometer and the crystallographic data in this study have been deposited in the Cambridge Structural Database under entry ID CCDC 2388594. The crystalline structure was explored on a Rigaku SmartLab X-ray diffractometer with Cu Kα radiation in a step of 0.01° and θ–2θ scan mode from 5° to 50°. Perovskite film morphology was examined by a high-resolution field emission scanning electron microscopy (SEM) (TESCAN VEGA3). Grazing-incidence wide-angle X-ray scattering (GIWAXS) was investigated using a Xeuss 2.0 SAXS/WAXS laboratory beamline with a Cu X-ray source (8.05 keV, 1.54 Å) and a Pilatus3R 300K detector. Time-resolved decay spectra were measured using a PL spectrometer (Edinburgh Instruments, FLS920) with the excitation source of 636.2 nm picosecond pulsed diode laser (EPL-635, ≈5 nJ cm^{-2}) and detected at 810 nm. Ultraviolet photoemission spectroscopy (UPS) measurement was carried out by a VG ESCLAB 220i-XL surface analysis system equipped with a monochromatic Al K X-ray source (1486.6 eV) in a vacuum of 3.0×10^{-8} Torr. For the completed devices, *J*–*V* curves were obtained using a Keithley 2400 Source Meter under standard AM 1.5 G illumination (Enli Technology Co. Ltd., Taiwan), and the light intensity was calibrated by a standard KG-5 Si diode. Both forward (from −0.2 to 1.25 V) and reverse scanning (from 1.25 to −0.2 V) were performed with a delay time of 100 ms. The active area of devices (0.09 cm^2) is confined by the crossed area of the counter electrode and FTO stripe, and the test area (0.04 cm^2) is typically defined by a metal mask with an aperture aligned with the active area. EQE spectra were measured with a QE-R 3011 EQE system (Enli Technology Co. Ltd., Taiwan) using 210 Hz chopped monochromatic light ranging from 300 to 850 nm. The EL EQE spectra were recorded by an LED photo-luminescence quantum yield measurement system (Enli Tech LQ-100) equipped with the Keithley 2400 Source Measure Unit. Mott–Schottky plotting was obtained at a frequency of 10 kHz with bias potential from 0 to 1.3 V. Thermal admittance spectroscopy (TAS) was performed via a capacitance–frequency measurement under an alternating current (AC) voltage (10 mV) with the frequency decreased from 10^6 to 1 Hz. Transient photovoltage (TPV) and transient photocurrent (TPC) measurements were performed using a self-designed system excited by a 532 nm (Brio, 20 Hz, 4 ns) pulse laser in the dark. A digital oscilloscope (Tektronix, DPO 7104) was used to record the photocurrent or photovoltage decay process.[62] Pulsed voltage (PV)-space–charge limited current (SCLC) measurement was carried out for the ETL-only devices with a structure of FTO/SnO_2/without or with MeOBTBT-POEt/Perovskite/[6,6]-phenyl-C61-butyric acid methyl ester (PCBM)/Ag. PV-SCLC testing are followed the protocol (pulsed bias voltage mode: pulse width is 20 ms, time between voltage pulses t_{bvp} is 5 min, V_{step} is 0.1 V both in forward and reverse scanning from 0 to 6 V, and from 6 to 0 V, respectively). Thermogravimetric analysis (TGA) measurements were conducted on TA Instruments Q600 SDT thermal analysis system under N_2 at a heating rate of 10 °C min^{-1}. Differential scanning calorimetry (DSC) measurements were conducted by using a TA Instruments Q2000 differential scanning calorimeter under N_2. ^{1}H NMR and ^{13}C NMR spectra were measured on Bruker AVANCE III 300 MHz and 400 MHz spectrometers. Mass spectra were recorded on a Bruker APEX IV mass spectrometer. The Raman mapping was performed with a Confocal Raman Microscope, WITec Alpha 300 R. The excitation wavelength of Raman spectroscopy is 532 nm.

Supporting Information

Supporting Information is available from the Wiley Online Library or from the author.

Acknowledgements

The authors gratefully acknowledge the support of the BL03HB beamline station of the Shanghai Synchrotron Radiation Facility on GIXD measurements. This work was supported by the Research Grants Council of Hong Kong (15307922, C7018-20G, C4005-22Y, C7082-21G, JLFS/P-701/24, SRFS2223-5S01, RFS2122-7S06, 3-RAE9), National Natural Science Foundation of China (52403250, 22425205), the Hong Kong Polytechnic University: Sir Sze-yuen Chung Endowed Professorship Fund (8-8480), RISE (U-CDC6), PRI (Q-CD7X), Start-up Fund for RAPs under the Strategic Hiring Scheme (1-BD1H, 1-BD4G), RI-iWEAR Strategic Supporting Scheme (1-CD94), Guangdong-Hong Kong-Macao Joint Laboratory for Photonic-Thermal-Electrical Energy Materials and Devices (GDSTC No. 2019B121205001), Croucher Foundation Senior Research Fellowship (2022), MHKJFS (MHP/178/23), ITF-TCFS (GHP/380/22GD) and ITF-ITSP (ITS/184/23) from ITC of Hong Kong, and the University Development Fund (UDF-01003793) by the Chinese University of Hong Kong, Shenzhen.

Conflict of Interest

The authors declare no conflict of interest.

Author Contributions

Z.W., Q.L., and M.L. contributed equally to this work. G.L., J.T., Z.W., M.L., and K.L. conceived the idea. G.L. and J.T. supervised the project. Z.W., Q.L., M.L., and K.L. designed the experiments and analyzed the data. G.S., T.Z., Y.H., Z.R., and J.Z. helped to make the devices. M.L. and H.X. conducted the electrostatic potential and dipole moment calculations. S.L. and X.L. performed the GIWAXS measurement. B.Y., R.M., D.L., L.Z., H.T.C., and L.C. helped to measure TPV, TPC, XPS, TRPL, and Raman spectroscopy. S.C. and C.Y. helped to measure ToF-SIMS. Z.W., Q.L., M.L., and K.L. collaborated to prepare the manuscript. R.A. helped to revise the manuscript. All authors discussed the results and commented on the manuscript.

Data Availability Statement

The data that support the findings of this study are available from the corresponding author upon reasonable request.

Keywords

buried interface, crystallization-driven template, dipole moment, nonradiative recombination, perovskite solar cells, S–Q limit, supramolecular assembly

Received: November 20, 2024
Revised: March 26, 2025
Published online: April 9, 2025

[1] B. Cai, Y. Xing, Z. Yang, W.-H. Zhang, J. Qiu, *Energy Environ. Sci.* **2013**, *6*, 1480.
[2] M. Grätzel, *Nat. Mater.* **2014**, *13*, 838.
[3] H.-S. Kim, C.-R. Lee, J.-H. Im, K.-B. Lee, T. Moehl, A. Marchioro, S.-J. Moon, R. Humphry-Baker, J.-H. Yum, J. E. Moser, *Sci. Rep.* **2012**, *2*, 591.
[4] P. Gao, M. Grätzel, M. K. Nazeeruddin, *Energy Environ. Sci.* **2014**, *7*, 2448.
[5] H. Lin, M. Yang, X. Ru, G. Wang, S. Yin, F. Peng, C. Hong, M. Qu, J. Lu, L. Fang, *Nat. Energy* **2023**, *8*, 789.
[6] N.-G. Park, H. Segawa, *ACS Photonics* **2018**, *5*, 2970.
[7] Z. W. Gao, Y. Wang, W. C. Choy, *Adv. Energy Mater.* **2022**, *12*, 2104030.
[8] S. Heo, G. Seo, Y. Lee, D. Lee, M. Seol, J. Lee, J.-B. Park, K. Kim, D.-J. Yun, Y. S. Kim, *Energy Environ. Sci.* **2017**, *10*, 1128.

[9] Z. Ren, K. Liu, H. Hu, X. Guo, Y. Gao, P. W. Fong, Q. Liang, H. Tang, J. Huang, H. Zhang, *Light Sci. Appl.* **2021**, *10*, 239.
[10] K. Liu, S. Chen, J. Wu, H. Zhang, M. Qin, X. Lu, Y. Tu, Q. Meng, X. Zhan, *Energy Environ. Sci.* **2018**, *11*, 3463.
[11] J. Chen, X. Zhao, S. G. Kim, N. G. Park, *Adv. Mater.* **2019**, *31*, 1902902.
[12] Z. Feng, X. Liu, T. Tian, Z. Zhu, R. Jiang, J. Li, Y. Yuan, J. Gong, G. Gao, J. Tong, Y. Peng, S. Bai, F. Huang, X. Xiao, P. Muller-Buschbaum, Y. B. Cheng, T. Bu, *Adv. Mater.* **2025**, *37*, 2412692.
[13] R. Azmi, W. T. Hadmojo, S. Sinaga, C. L. Lee, S. C. Yoon, I. H. Jung, S. Y. Jang, *Adv. Energy Mater.* **2017**, *8*, 1701683.
[14] R. Azmi, S. Zhumagali, H. Bristow, S. Zhang, A. Yazmaciyan, A. R. Pininti, D. S. Utomo, A. S. Subbiah, S. De Wolf, *Adv. Mater.* **2024**, *36*, 2211317.
[15] D. S. Utomo, L. M. Svirskaite, A. Prasetio, V. Malinauskiene, P. Dally, E. Aydin, A. Musiienko, V. Getautis, T. Malinauskas, R. Azmi, S. De Wolf, *ACS Energy Lett.* **2024**, *9*, 1682.
[16] Q. Liang, K. Liu, Y. Han, H. Xia, Z. Ren, D. Li, T. Zhu, L. Cheng, Z. Wang, C. Zhu, P. W. K. Fong, J. Huang, Q. Chen, Y. Yang, G. Li, *Nat. Commun.* **2025**, *16*, 190.
[17] C. Xu, P. Hang, C. Kan, X. Guo, X. Song, C. Xu, G. You, W. Q. Liao, H. Zhu, D. Wang, Q. Chen, Z. Hong, R. G. Xiong, X. Yu, L. Zuo, H. Chen, *Nat. Commun.* **2025**, *16*, 835.
[18] B. Dong, M. Wei, Y. Li, Y. Yang, W. Ma, Y. Zhang, Y. Ran, M. Cui, Z. Su, Q. Fan, Z. Bi, T. Edvinsson, Z. Ding, H. Ju, S. You, S. M. Zakeeruddin, X. Li, A. Hagfeldt, M. Grätzel, Y. Liu, *Nat. Energy* **2025**, *10*, 342.
[19] X. Zhang, Y. Wang, K. Zhang, M. Tao, H. Guo, L. Guo, Z. Song, J. Wen, Y. Yang, Y. Hou, Y. Song, *Angew. Chem. Int. Ed. Engl.* **2025**, *64*, 202423827.
[20] M. Li, M. Liu, F. Qi, F. R. Lin, A. K. Jen, *Chem. Rev.* **2024**, *124*, 2138.
[21] R. Azmi, D. S. Utomo, B. Vishal, S. Zhumagali, P. Dally, A. M. Risqi, A. Prasetio, E. Ugur, F. Cao, I. F. Imran, A. A. Said, A. R. Pininti, A. S. Subbiah, E. Aydin, C. Xiao, S. Il Seok, S. De Wolf, *Nature* **2024**, *628*, 93.
[22] H. Chen, M. Li, Z. Lu, X. Wang, J. Yang, Z. Wang, F. Zhang, C. Gu, W. Zhang, Y. Sun, *Nat. Commun.* **2019**, *10*, 3872.
[23] M. Li, M. Rogatch, H. Chen, X. Guo, J. Tang, *Acc. Mater. Res.* **2024**, *5*, 505.
[24] M. Li, T. Jiang, X. Wang, H. Chen, S. Li, F. Wei, Z. Ren, S. Yan, X. Guo, H. Tu, *J. Mater. Chem. C* **2020**, *8*, 2155.
[25] J. Yang, D. Yan, T. S. Jones, *Chem. Rev.* **2015**, *115*, 5570.
[26] D. He, Y. Pan, H. Nan, S. Gu, Z. Yang, B. Wu, X. Luo, B. Xu, Y. Zhang, Y. Li, *Appl. Phys. Lett.* **2015**, *107*, 183103.
[27] G. Giri, E. Verploegen, S. C. Mannsfeld, S. Atahan-Evrenk, D. H. Kim, S. Y. Lee, H. A. Becerril, A. Aspuru-Guzik, M. F. Toney, Z. Bao, *Nature* **2011**, *480*, 504.
[28] K. Liu, Q. Liang, M. Qin, D. Shen, H. Yin, Z. Ren, Y. Zhang, H. Zhang, P. W. Fong, Z. Wu, *Joule* **2020**, *4*, 2404.
[29] R. Wang, J. Xue, L. Meng, J.-W. Lee, Z. Zhao, P. Sun, L. Cai, T. Huang, Z. Wang, Z.-K. Wang, Y. Duan, J. L. Yang, S. Tan, Y. Yuan, Y. Huang, Y. Yang, *Joule* **2019**, *3*, 1464.
[30] Y. Chen, Q. Meng, Y. Xiao, X. Zhang, J. Sun, C. B. Han, H. Gao, Y. Zhang, Y. Lu, H. Yan, *ACS Appl. Mater. Interfaces* **2019**, *11*, 44101.
[31] T. J. Jacobsson, J.-P. Correa-Baena, E. Halvani Anaraki, B. Philippe, S. D. Stranks, M. E. Bouduban, W. Tress, K. Schenk, J. Teuscher, J.-E. Moser, *J. Am. Chem. Soc.* **2016**, *138*, 10331.
[32] Y. Ma, X. Du, R. Chen, L. Zhang, Z. An, A. K. Y. Jen, J. You, S. Liu, *Adv. Mater.* **2023**, *35*, 2306947.
[33] S. Dudarev, *Phys. Rev. B* **2000**, *62*, 9325.
[34] L. Qiu, Z. Liu, L. K. Ono, Y. Jiang, D. Y. Son, Z. Hawash, S. He, Y. Qi, *Adv. Funct. Mater.* **2019**, *29*, 1806779.
[35] H. Yu, H. I. Yeom, J. W. Lee, K. Lee, D. Hwang, J. Yun, J. Ryu, J. Lee, S. Bae, S. K. Kim, *Adv. Mater.* **2018**, *30*, 1704825.
[36] K. Choi, J. Lee, H. I. Kim, C. W. Park, G.-W. Kim, H. Choi, S. Park, S. A. Park, T. Park, T. Stable, *Energy Environ. Sci.* **2018**, *11*, 3238.
[37] M. Maiberg, T. Hölscher, S. Zahedi-Azad, R. Scheer, *J. Appl. Phys.* **2015**, *118*, 105701.
[38] B. Wu, H. T. Nguyen, Z. Ku, G. Han, D. Giovanni, N. Mathews, H. J. Fan, T. C. Sum, *Adv. Energy Mater.* **2016**, *6*, 1600551.
[39] Q. Liang, K. Liu, M. Sun, Z. Ren, P. W. Fong, J. Huang, M. Qin, Z. Wu, D. Shen, C. S. Lee, *Adv. Mater.* **2022**, *34*, 2200276.
[40] M. Saliba, T. Matsui, K. Domanski, J.-Y. Seo, A. Ummadisingu, S. M. Zakeeruddin, J.-P. Correa-Baena, W. R. Tress, A. Abate, A. Hagfeldt, *Science* **2016**, *354*, 206.
[41] Q. Jiang, Y. Zhao, X. Zhang, X. Yang, Y. Chen, Z. Chu, Q. Ye, X. Li, Z. Yin, J. You, *Nat. Photonics* **2019**, *13*, 460.
[42] W. Tress, N. Marinova, O. Inganäs, M. K. Nazeeruddin, S. M. Zakeeruddin, M. Graetzel, *Adv. Energy Mater.* **2015**, *5*, 1400812.
[43] U. Rau, *Phys. Rev. B* **2007**, *76*, 085303.
[44] D. Credgington, J. R. Durrant, *J. Phys. Chem. Lett.* **2012**, *3*, 1465.
[45] Y. Li, Y. Li, J. Shi, H. Li, H. Zhang, J. Wu, D. Li, Y. Luo, H. Wu, Q. Meng, *Appl. Phys. Lett.* **2018**, *112*, 053904.
[46] E. A. Duijnstee, J. M. Ball, V. M. Le Corre, L. J. A. Koster, H. J. Snaith, J. Lim, *ACS Energy Lett.* **2020**, *5*, 376.
[47] P. Murgatroyd, *J. Phys. D Appl. Phys.* **1970**, *3*, 151.
[48] S. Tan, I. Yavuz, M. H. Weber, T. Huang, C.-H. Chen, R. Wang, H.-C. Wang, J. H. Ko, S. Nuryyeva, J. Xue, *Joule* **2020**, *4*, 2426.
[49] B. Chen, P. N. Rudd, S. Yang, Y. Yuan, J. Huang, *Chem. Soc. Rev.* **2019**, *48*, 3842.
[50] X. Zheng, B. Chen, J. Dai, Y. Fang, Y. Bai, Y. Lin, H. Wei, X. C. Zeng, J. Huang, *Nat. Energy* **2017**, *2*, 17102.
[51] Z. Wang, Z. Han, X. Chu, H. Zhou, S. Yu, Q. Zhang, Z. Xiong, Z. Qu, H. Tian, W. Wang, F. Wan, Y. Yuan, Y. Lin, Y. Yang, X. Zhang, Q. Jiang, J. You, *Adv. Mater.* **2024**, *36*, 2407681.
[52] X. Hu, N. Shen, D. Zhang, Y. Wu, R. Shang, L. Wang, C. Qin, *Adv. Mater.* **2024**, *36*, 2313099.
[53] D. Liu, C. Chen, X. Wang, X. Sun, B. Zhang, Q. Zhao, Z. Li, Z. Shao, X. Wang, G. Cui, S. Pang, *Adv. Mater.* **2024**, *36*, 2310962.
[54] J. J. Yoo, G. Seo, M. R. Chua, T. G. Park, Y. Lu, F. Rotermund, Y. K. Kim, C. S. Moon, N. J. Jeon, J. P. Correa-Baena, V. Bulovic, S. S. Shin, M. G. Bawendi, J. Seo, *Nature* **2021**, *590*, 587.
[55] W. Peng, K. Mao, F. Cai, H. Meng, Z. Zhu, T. Li, S. Yuan, Z. Xu, X. Feng, J. Xu, M. D. McGehee, J. Xu, *Science* **2023**, *379*, 683.
[56] G. Yang, Z. Ren, K. Liu, M. Qin, W. Deng, H. Zhang, H. Wang, J. Liang, F. Ye, Q. Liang, H. Yin, Y. Chen, Y. Zhuang, S. Li, B. Gao, J. Wang, T. Shi, X. Wang, X. Lu, H. Wu, J. Hou, D. Lei, S. K. So, Y. Yang, G. Fang, G. Li, *Nat. Photonics* **2021**, *15*, 681.
[57] J. Jeong, M. Kim, J. Seo, H. Lu, P. Ahlawat, A. Mishra, Y. Yang, M. A. Hope, F. T. Eickemeyer, M. Kim, Y. J. Yoon, I. W. Choi, B. P. Darwich, S. J. Choi, Y. Jo, J. H. Lee, B. Walker, S. M. Zakeeruddin, L. Emsley, U. Rothlisberger, A. Hagfeldt, D. S. Kim, M. Gratzel, J. Y. Kim, *Nature* **2021**, *592*, 381.
[58] M. Kim, J. Jeong, H. Lu, T. K. Lee, F. T. Eickemeyer, Y. Liu, I. W. Choi, S. J. Choi, Y. Jo, H.-B. Kim, S.-I. Mo, Y.-K. Kim, H. Lee, N. G. An, S. Cho, W. R. Tress, S. M. Zakeeruddin, A. Hagfeldt, J. Y. Kim, M. Grätzel, D. S. Kim, *Science* **2022**, *375*, 302.
[59] Y. Zhao, F. Ma, Z. Qu, S. Yu, T. Shen, H.-X. Deng, X. Chu, X. Peng, Y. Yuan, X. Zhang, J. You, *Science* **2022**, *377*, 531.
[60] Z. Huang, Y. Bai, X. Huang, J. Li, Y. Wu, Y. Chen, K. Li, X. Niu, N. Li, G. Liu, Y. Zhang, H. Zai, Q. Chen, T. Lei, L. Wang, H. Zhou, *Nature* **2023**, *623*, 531.
[61] J. Zhu, S. Park, O. Y. Gong, C. Sohn, Z. Li, Z. Zhang, B. Jo, W. Kim, G. S. Han, D. H. Kim, T. K. Ahn, J. Lee, H. S. Jung, *Energy Environ. Sci.* **2021**, *14*, 4903.
[62] J. Shi, D. Li, Y. Luo, H. Wu, Q. Meng, *Rev. Sci. Instrum.* **2016**, *87*, 123107.